Additive Manufacturing of Hall Thruster Magnetic Circuits

IEPC-2024-431

Presented at the 38th International Electric Propulsion Conference, Toulouse, France
June 23-28, 2024

Francesco Marconcini[*], Luciano C. Manzolillo[†], Guido Giammarinaro[‡], Carla Guidi[§],
Manuel M. Saravia[¶], Francesco Tamburrino[‖], Armando V. Razionale[**], Fabrizio Paganucci[††]
University of Pisa, Pisa, 56122, Italy

Giulia Becatti[‡‡]
University of Stuttgart, Stuttgart, 70569, Germany

Tommaso Andreussi
Sant'Anna School of Advanced Studies, Pisa, 56127, Italy

Abstract: Hall thrusters are one of the most widely used electric propulsion systems, primarily due to their relatively high thrust-to-power ratio and simple architecture. Despite the high technology readiness level reached in recent years, there is still significant room for improvements in performance, structural design and thermal management. In this sense, a crucial role could be played by the additive manufacturing (AM) of magnetic circuits. This component is fundamental for the functioning of the thruster, as the magnetic field topology and intensity are key variables for controlling discharge stability, ion acceleration, and channel erosion phenomena. Additionally, the magnetic circuit serves as the support structure for the majority of the other thruster components. The freedom in design and the possibilities to reduce mass, consolidate components, and optimize thermal management offered by AM open the doors to the creation of more efficient and robust thrusters. Moreover, the rapid prototyping capability and reduced production costs allow for economic and quick testing, accelerating scientific progress in this field. This article aims to present the progress made in developing an additive manufacturing procedure for magnetic circuits of Hall thrusters. The procedure is based on material extrusion additive manufacturing (MEAM) of polymeric feedstocks highly filled with metal powders and allows for the production of a fully metallic component through the three steps of printing, debinding and sintering. The article presents the results obtained with two soft iron filaments, one commercial and the other specially developed. The latter has shown high shape retention after sintering, relative densities above 92%, and magnetic properties comparable to those of non-annealed ARMCO iron. The effectiveness of the technique is demonstrated through the realization of the magnetic circuit of a low-power thruster. Despite the relatively low densification and deformation during sintering, there is significant room for improvement by optimizing process parameters and feedstock. Even at its current state, the technique can be used to produce functional components with equipment costs

[*]Ph.D. Student, Department of Information Engineering, francesco.marconcini@phd.unipi.it
[†]Test Engineer Intern, Aerospazio Tecnologie SRL, luciano.manzolillo@aerospazio.com
[‡]Ph.D. Student, Department of Information Engineering, guido.giammarinaro@phd.unipi.it
[§]Ph.D. Student, Department of Information Engineering, carla.guidi@phd.unipi.it
[¶]Researcher, Department of Civil and Industrial Engineering, manuel.saravia@ing.unipi.it
[‖]Researcher, Department of Civil and Industrial Engineering, francesco.tamburrino@unipi.it
[**]Professor, Department of Civil and Industrial Engineering, armando.viviano.razionale@unipi.it
[††]Professor, Department of Civil and Industrial Engineering, fabrizio.paganucci@unipi.it
[‡‡]Researcher, Institute of Space Systems, becattig@irs.uni-stuttgart.de
Professor, Institute of Mechanical Intelligence, tommaso.andreussi@santannapisa.it

around 10 k€ . This makes it extremely competitive compared to other metal additive manufacturing techniques and accessible to small laboratories that can contribute to the development of next generation of high-performance Hall thrusters.

Nomenclature

HT	= Hall Thruster
UniPi	= University of Pisa
AM	= Additive Manufacturing
SFM	= Soft Ferromagnetic Materials
MEAM	= Material Extrusion Additive Manufacturing
TRL	= Tecnology Readiness Level
LPBF	= Laser Powder Bed Fusion
DED	= Direct Energy Deposition
TVF-PI	= The Virtual Foundry's Pure Iron Filament
NaMEX-Fe	= Costum developed soft iron filament
FFF	= Fused Filament Fabrication
PLA	= Polylactic Acid
SEM	= Scanning Electron Microscopy
PEI	= Polyethylenimine
SPT	= Stationary Plasma Thruster
TAL	= Thruster with Anode Layer
MIC	= Mineral Insulated Cables
H	= Magnetic field
H_c	= Coercitivity
B	= Magnetic flux density
B_M	= Magnetization saturation
D_m	= Average diameter of the toroidal specimen
N	= Number of winding in a coil
b	= Channel width
d	= Channel mean diameter
L	= Channel length
B_r	= Radial magnetic field peak valued along the median line of the channel
n	= Plasma density
P_D	= Discharge power
V_D	= Discharge voltage
I_{sp}	= Anodic specific impulse
η_T	= Anodic thrust efficiency
$\dot{m}$	= Anodic mass flow rate

I. Introduction

A. Hall Thruster Magnetic Circuits

The Hall thruster (HT) magnetic circuit is a soft ferromagnetic component primarily responsible for channeling the magnetic flux generated by coils or permanent magnets to establish an appropriate magnetic field in the region where the plasma is produced. The topology and intensity of this magnetic field are crucial for generating and maintaining the discharge and for controlling ion acceleration and channel erosion phenomena. Additionally, the magnetic circuit supports other thruster components, protecting them from the space environment and the plume, and providing a surface for the radiative thermal dissipation of heat generated in the channel or the cathode. Hereinafter, we will always refer to the classical configuration of the Hall thruster with a discharge channel made of dielectric material, sometimes referred to as SPT (Stationary Plasma Thruster). However, most considerations are also valid for the TAL (Thruster with Anode Layer) configuration.

Currently, the typical design of a Hall thruster magnetic circuit consists of an arrangement of thin cylindrical elements connected to a rear plate, as shown in Figure 1. Figure 2 shows a simplified drawing of generic magnetic circuits with coils and permanent magnets in magnetic shielding and classical configurations, illustrating also the magnetic flux lines and the radial magnetic field value along the channel centerline. Real magnetic circuits often incorporate thickenings, chamfers, and windows in various components to adjust the magnetic field topology, reduce mass, and maximize radiative thermal dissipation.

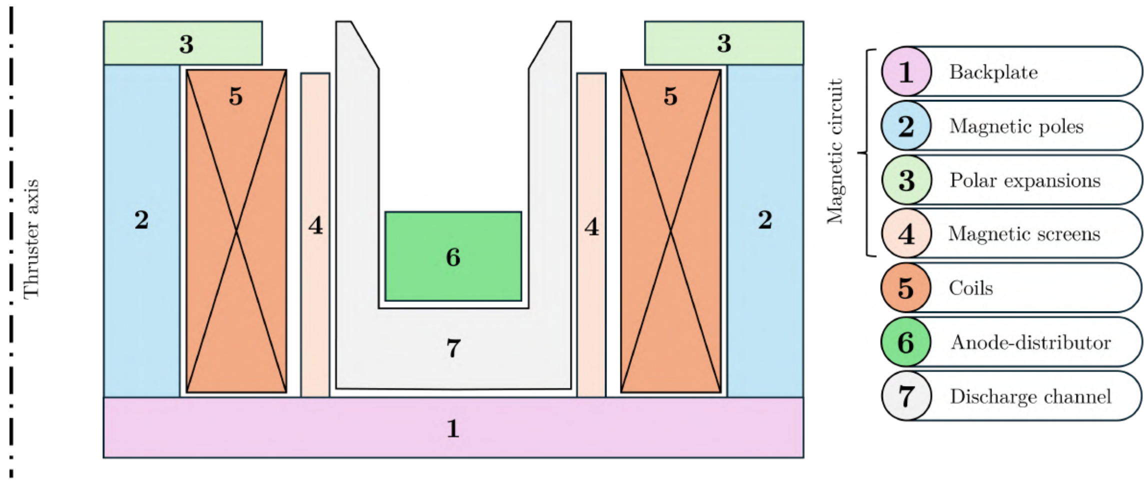

Figure 1. Common architecture of a Hall thruster magnetic circuit.

Electromagnets are usually preferred over permanent magnets due to the possibility of adjusting the magnetic field for different thruster operating modes. They can also be operated with reversed currents to counterbalance any torque generated by a small azimuthal velocity component of the ions.[1] On the other hand, permanent magnets are generally more compact, given the same magnetomotive force, allowing for lighter circuits since they do not occupy radial space, require no electrical power, and do not produce ohmic heating. This directly increases total thrust efficiency, reduces mass, and can potentially lower the mass of any thermal management system. However, they are very fragile, requiring encapsulation techniques for installation on the thruster, and they cannot be turned off. This is generally undesirable since the magnetic fields generated by the thruster can interfere with the operation of other spacecraft subsystems or instruments, even when the spacecraft is not performing orbital manoeuvres. Both magnetic flux generation systems are susceptible to performance degradation at high temperatures. Coils need increasing power with rising temperature due to resistivity increase and are also subject to insulation melting at very high temperatures, which can lead to short circuits. For this reason, Mineral-Insulated Cables (MIC), which can operate up to 700°C, are used in most cases. High-temperature polymer-insulated cables are also being developed but, currently, they cannot exceed 300°C.[2] Conversely, permanent magnets are characterized by a reversible degradation of the remanence field, which becomes irreversible once the Curie temperature of the material is exceeded. Samarium-cobalt magnets, capable of operating at temperatures up to 550°C,[3] are generally used for Hall thruster applications. They offer a good combination of high magnetic field strength (high remanence), high resistance to demagnetization (high coercivity), and high energy density (high maximum energy product) compared to other hard ferromagnetic materials. Recently, new materials with improved performance have been emerging,[3] but their application in the propulsion field is currently limited.

It is worth noting that hybrid configurations using both coils and permanent magnets have been proposed or implemented in thrusters. In addition, in the figures, the coils are uniformly distributed azimuthally, but discretized external coils are also commonly used. This approach allows for simpler manufacturing but generally has the drawbacks of creating greater radial bulk, requiring precise dimensioning to achieve azimuthal uniformity of the magnetic field, and making simulations more challenging due to the lack of axial symmetry. The same applies to permanent magnets, which are usually used as discretized rods or cuboids. Moreover, for magnetic shielding configurations, a *trim* coil is often used to adjust the position of the magnetic field separatrix in the channel, effectively controlling the radial magnetic field gradient.

From Figure 2, several desired characteristics for the magnetic field of Hall thrusters can be inferred. Firstly, it is observed that the field near the channel exit is approximately radial. This is the basis of the working principle of a Hall thruster, in which the radial magnetic field together with an axial electric field reduces electron mobility near the end of the channel. The peak value of the magnetic field is chosen to magnetize electrons but not ions within the channel. This is crucial for the thruster's operation, as the reduced electron mobility creates a potential drop in the plasma, accelerating the unmagnetized ions and thereby generating thrust. The peak value is selected so that the characteristic Larmor radius of electrons is much smaller than the characteristic dimensions of the discharge channel. For thrusters with nominal discharge power around 1 kW the typical field strength used is around 200 G, whereas higher values are usually employed for smaller thrusters. Since this parameter is critical for thruster functioning, the circuit design must allow precise adjustment of the radial magnetic field peak value over a relatively wide range to maximize thruster performance across all operating conditions.

From Figure 2, we note also that even for an unshielded circuit the magnetic field lines are not perfectly radial. This is because the magnetic field curvature focuses ion trajectories towards the thruster's centerline, reducing beam divergence and wall erosion.[4] This effect is commonly referred to as a plasma lens, but to be effective, the magnetic field topology must remain symmetric about the channel centerline. The plasma lens can be considered a precursor to the magnetic shielding technique. The technique is based on the concept of thermalized potential: assuming uniform electron temperature along a magnetic field line and a sufficiently small plasma density gradient, it can be demonstrated that the potential along that line remains constant, hence magnetic field lines also act as equipotential lines in the plasma, and so the electric field is perpendicular to them. In shielded Hall thrusters, the principle of thermalized potential is utilized by shaping magnetic field lines to penetrate the channel nearly parallel to the walls and extend almost to the anode. This unique magnetic topology affects the plasma in several ways:

- Due to the equipotentiality of magnetic lines, the electric field directs ions away from the channel walls, drastically reducing the flux of ions with high energy or steep incidence angles.
- Cold electrons from the anode region move along magnetic lines, creating a protective layer along the channel walls, thus lowering the sheath potential.
- The high electron temperature region is shifted downstream reducing again the number and energy of ions colliding with channel walls.

Using this technique we can obtain a three-order of magnitude decrease in erosion rate, thus the ceramic channel walls no longer determine the maximum operational life of Hall thrusters. Figure 2 illustrates the difference between the two topologies. To implement magnetic shielding topology, screens are typically brought closer to the channel exit, thickened, and polar expansions reduced. This usually requires greater magnetomotive force compared to non-shielded configurations to achieve the same peak radial field in the channel. Additionally, trim coils are often necessary to maximize shielding. While non-shielded thrusters can be used for missions with low total impulse, shielding reduces performance variations in thruster operational life due to progressive channel geometry changes from erosion. Recent studies have also explored using metallic or graphite materials for the channel,[5] enhancing mechanical performance and resistance to exotic propellants. Therefore, nearly all next-generation thrusters are implementing this new topology. Despite it can be generally observed a slight performance reduction in shielded thrusters compared to unshielded

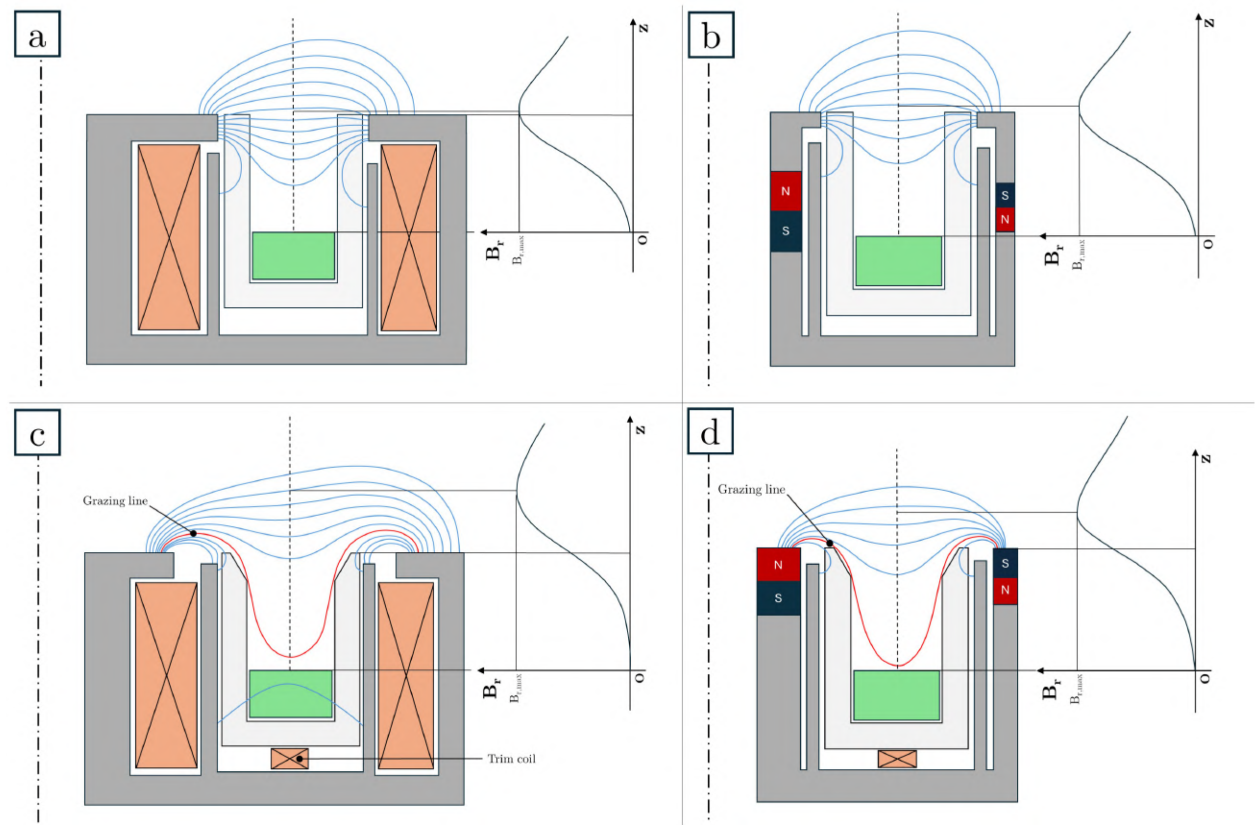

Figure 2. Typical classic magnetic circuit configuration, with coils (a) and permanent magnets (b), and magnetic shielding circuit configuration with coils (c) and permanent magnets (d). The magnetic flux streamlines are represented in blue, whereas, on the right of each configuration, a plot of the radial magnetic flux density along the median line of the channel with the distance from the anode is shown.

ones for given operational parameters and thruster geometry, this gap could potentially be minimized in the future through further topology refinements.

Another fundamental parameter for thruster topology is the axial gradient of the radial magnetic field along the discharge channel's centerline. Research, notably by Morozov, has shown that plasma oscillations are minimized with a positive magnetic field gradient ($\nabla B > 0$), where the field increases from the anode towards the channel exit, reaching its peak. Not only the sign but also the magnitude of this gradient significantly impacts performance. Several studies have identified an optimal gradient that enhances ion focusing and reduces plume divergence. This gradient is closely linked to the position and thickness of the acceleration region. The introduction of magnetic screens in second-generation Hall thrusters aimed to increase ∇B, creating a region of low magnetic fields at the anode. Despite these discoveries being made over 40 years ago the effects of varying magnetic field gradients remain an active area of research.

Iron or low-carbon steel can be used as materials for the magnetic circuit, but cobalt-iron (Co-Fe) alloys are preferred due to their exceptional magnetic saturation, high permeability, elevated Curie temperature, and strength. It is important to note that despite the advantages in magnetic performance, machining high-performance iron-cobalt alloys presents inherent challenges due to their poor machinability. Moreover, obtaining wrought materials for large thrusters is both demanding and costly, as Co-Fe alloys are typically available only in sheet form. Additionally, iron-cobalt alloys have a thermal conductivity of about 40% lower than pure iron and are more expensive. Table 1 presents some of the key physical characteristics of these materials, with Hiperco 50 being an iron-cobalt alloy. Regarding iron, to avoid interpretation errors, according to ASTM standards, *pure iron* denotes a material with purity exceeding 99.9% and carbon content below 60 ppm,[6] *soft iron* denotes a material with purity exceeding 99.4% and carbon content below 300 ppm,[7] while *low carbon steel* denotes a material with purity exceeding 98.5% and carbon content below 200 ppm.[8] Definitions vary depending on standards, and terms are often used interchangeably.

Material	Saturation magnetization [T]	Curie Temperature [°C]	Max Relative Permeability	Thermal Conductivity (25°C) [W/m*K]	Density [kg/m^3]	Coefficient of Linear Thermal Expansion	0.2% Yield Strength [MPa]
ARMCO pure iron	2.16	770	19000	73.2	7860	13.7	138-186
Hiperco 50	2.45	940	7000-15000	32	8120	9.4	250-450

Table 1. Key physical characteristics of ARMCO pure iron and Hiperco 50.[9–11]

B. Additive Manufacturing of Magnetic Circuits

Additive Manufacturing (AM) is defined by ISO/ASTM as *the process of joining materials to create parts from 3D model data, usually layer upon layer, as opposed to subtractive and formative manufacturing methodologies*.[12] AM offers numerous advantages over traditional subtractive techniques, including unparalleled design flexibility, diminished material wastage, the possibility of part consolidation, and faster production cycles for complex components, all factors leading to a decrease in production expenses.[13]

A wide range of techniques for 3D printing of metallic materials are nowadays available and can classified based on different criteria. The most commonly used ones are:

- **Powder Bed Fusion (PBF)**: A heat source is used to selectively melt and fuse metal powder layers. Based on the heat source, we identify:
  - **Selective Laser Melting (SLM)**: also known as Laser PBF (LBPF), uses a laser to melt the material.
  - **Electron Beam Melting (EBM)**: uses an electron beam in a vacuum to melt the material.
- **Directed Energy Deposition (DED)**: Metal is deposited by melting wire or powder with a focused energy source. Based on the heat source and the feedstock material, we identify:
  - **Laser Metal Deposition (LMD)**: Uses a laser to melt and deposit powder material.
  - **Electron Beam Additive Manufacturing (EBAM)**: Uses an electron beam to melt and deposit powder material.
  - **Wire Arc Additive Manufacturing (WAAM)**: Utilizes an electric arc to melt a metallic wire.
- **Binder Jetting**: Layers of metal powder are bound with a polymeric binder and then thermally debound and sintered.
- **Sheet Lamination**: Metal sheets together are cut and bonded together, often with ultrasonic welding.
- **Material Extrusion**: Metal-infused filaments, rods or pellets are extruded trough a heated nozzle, then the polymeric part of the printed component is removed and the part is sintered.

AM is now also widely used in the field of space propulsion, with DED being applied to produce chemical thruster nozzles and tanks (sometimes entire rockets),[14] and LPBF being widely used commercially for producing a variety of components.

Regarding Hall thruster magnetic circuits the utilization of AM could bring significant improvements. The layer-by-layer production not only offers a remedy to machining-induced magnetic property degradation and deformations but also inherently minimizes material waste. This can greatly reduce costs and production times since the machining of magnetic circuit components often results in significant material waste (over 80%) due to the shape of the circuit. Additionally, AM allows to avoid the machining of large cylindrical components with a significant thickness-to-diameter ratio, such as magnetic screens, which may result in substantial distortion of the piece or the onset of vibration problems. AM enables also the use of a broader range of materials, which can be obtained in a more flexible and economically advantageous powder form.

This can solve the previously described problem related to the poor machinability of iron-cobalt alloys, allowing their widespread use for the production of high-performance magnetic circuits.

AM also brings other important advantages, such as unparalleled design freedom, a reduction in production time and costs, and the possibility of part consolidation. This newfound design flexibility facilitates the development of innovative configurations and geometries for magnetic circuits. This in turn can lead to minimized power requirements for coils, reduced circuit mass and footprint, especially when adopted together with topology optimization strategies.

AM can also represent a paradigm shift in thermal management thanks to the possibility of integrating passive cooling systems or cooling channels into the magnetic circuit, as well as optimizing the shape for better heat dissipation by radiation, potentially also using multi-material printing techniques.

Other advantages of AM include the possibility of integrating diagnostics and optimizing interfaces with other thruster components.

The main issue in additive manufacturing of magnetic circuits is the low TRL currently associated with the printing of soft magnetic materials. Significant progress has been made in printing materials used in electric machines, such as iron-silicon alloys.[15,16] However, research lags for materials like iron-cobalt alloys, low-carbon steels or pure iron. Moreover, these materials are not often offered by the vast majority of companies in the sector.

C. State of the Art of Additively Manufactured Magnetic Circuits

There are very few examples available in the Literature of printed magnetic circuit applications for Hall thrusters. One of the more detailed works concerns the ASTREUS (Ascendant Sub-kW Transcelestial Electric Propulsion System) propulsion system developed by the Jet Propulsion Laboratory (JPL),[17] currently being commercialized under the name Halo12 by Exo Terra. ASTREUS is a Hall thruster operating between 200 and 1350 W, based on the MaSmi thruster also developed by JPL. It has demonstrated thrust up to 70 mN with an overall efficiency exceeding 50% and a total impulse of 1.5 MNs.[18] The motor's magnetic circuit was printed using DED in Hiperco 50 (49%Fe-49%Co-2%V) as recently detailed in a patent.[19] The circuit consists of four components: the main part, inner and outer pole expansions, and screens, shown all together during manufacturing in Figure 3a. Components were post-processed after printing to enhance surface finish and incorporate features such as windows in the outer pole and holes for inter-component connections. The magnetic performance of the circuit has shown to be within 5% of a traditionally manufactured circuit of the same material.[20]

Another thruster implementing a 3D-printed magnetic circuit is the H10, a high-power magnetically shielded motor under development at JPL, representing the successor to well-known H6 and H9. The thruster features a Hiperco magnetic circuit with integrated pulsating heat pipes, which enhance the thermal conductivity of the material by up to a factor of 20.[21] Figure 3b depicts the thruster, showcasing its distinctive external shape with protrusions, likely designed to enhance radiative heat dissipation.

Finally, Busek Inc.'s BHT-200 thruster, shown in Figure 3c, has also recently implemented a 3D-printed magnetic circuit. While detailed information is not publicly available, there exists a final summary report of the Small Business Innovation Research (SBIR) Phase 1 project titled *3D Printing Magnetic Circuit Components for Hall Effect Thrusters*.[22] The project explored both binder jetting and arc-welding techniques for advanced magnetic alloys, with arc welding selected for further study in Phase II. This technique is likely used for producing part of the thruster magnetic circuit.

D. Objective of the Work

The objective of this work is to present the progress made in developing a procedure for additively manufacturing magnetic circuits for Hall thrusters entirely within the University of Pisa (UniPi).

The AM procedure is based on Material Extrusion Additive Manufacturing (MEAM) and has been optimized in this initial phase for producing components in soft iron. Details regarding the material used and the production process are described in Section II, together with a discussion about the potential of the technique, its merits, and challenges. Section III demonstrates the capabilities of the technique, used with the design methods available in UniPi, through the fabrication of an additively manufactured magnetic circuit for a low-power Hall thruster. The circuit was assembled and its magnetic field is planned to be measured with a specially developed magnetic field mapper. The conclusions summarize the results obtained, highlight key findings, and outline the plans of the research group on the topic.

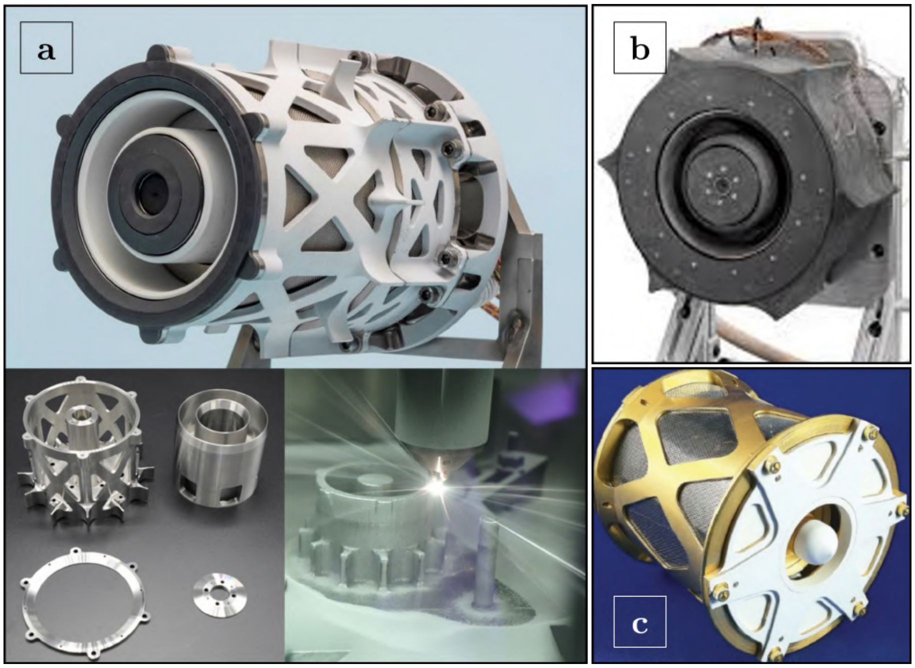

Figure 3. ASTREUS thruster with the various magnetic circuit components (a),[18] JPL H10 (b),[21] and Busek BHT-200 (c).

II. Progress in Material Extrusion Additive Manufacturing of Soft Ferromagnetic Materials at UniPi

A. Context of the Activity

To explore the potential of additive manufacturing for producing magnetic circuits for Hall thrusters, the first step is to access a production process that allows obtaining materials with properties as close as possible to those made with traditional manufacturing. This process should be cost-effective in terms of both equipment and materials, safe, fast, and easy to manage. Unfortunately, as mentioned earlier, the commercial use of soft ferromagnetic materials in widely adopted printing techniques such as PBF or DED is not yet widespread. Collaborating with an industrial partner to test a new material is possible but involves significant costs and times, logistical challenges due to limited access to the production systems, and often restrictions on the results that can be disclosed. Utilizing existing University systems has proven equally challenging. The Department of Civil and Industrial Engineering at UniPi has a LPBF printer (Renishaw REN AM 500E), but the need to purchase large quantities of metal powder and logistical issues related to the necessity of alternating different materials have discouraged further pursuit in this direction.

Fortunately, there is a technique that meets the logistical and budgetary needs of a small laboratory while enabling the production of high-performance components: Metal-Filled Feedstock Material Extrusion Additive Manufacturing (MFF-MEAM). In MFF-MEAM, a feedstock in the form of filament, pellet, or rod, consisting of a blend of polymers (binder) and metal particles, is extruded through a nozzle heated above the melting temperature of the binder. Subsequently, the 3D-printed *green parts* undergo debinding and sintering using the same process employed in Metal Injection Molding (MIM), as shown in Figure 4. In the first phase, debinding is carried out in solvents or in an acidic atmosphere to remove the initial polymer component, creating the so-called *brown part*, where the powders are held together only by the so-called *backbone polymer*. Subsequently, this component is removed through thermal debinding, followed often in the same furnace by sintering treatment, which ultimately produces a fully densified component albeit with isotropic shrinkage (10-15%) compared to the green part. Compared to more established techniques like LPBF, Binder Jetting, or DED, MEAM produces parts with lower resolution (100-600 μm compared to 20-200 μm for PBF) and higher porosity (relative density of 90-99% compared to >99% for PBF). However, MEAM also reduces safety concerns related to powder handling and requires significantly lower costs for feedstock and equipment, as

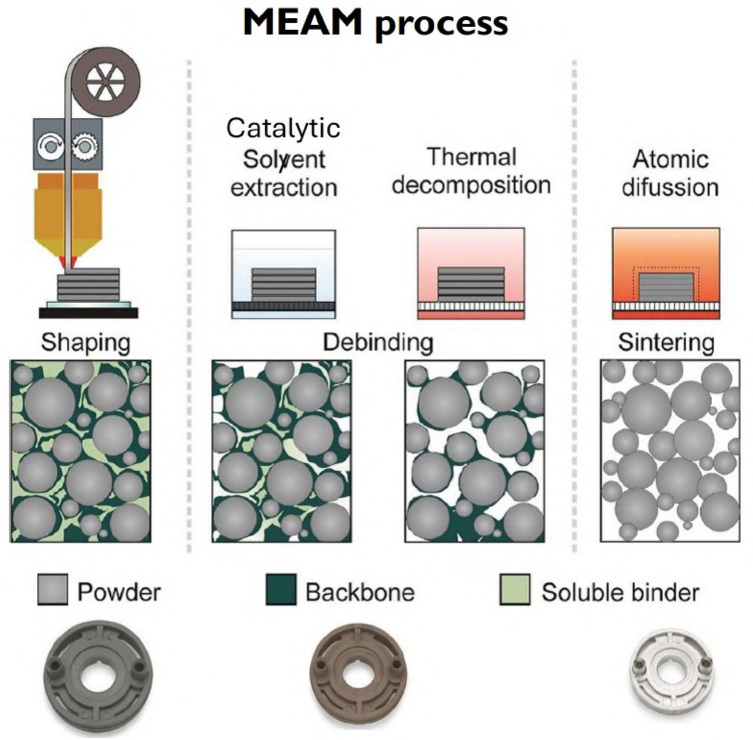

Figure 4. Metal filled feedstock material extrusion AM process.

even common desktop 3D printers can be used. Additionally, it offers greater flexibility in material changes and the production of multi-material parts.[23,24] MMF-MEAM has been applied to a wide range of metallic materials and has reached a technological level such as metal-filled filament feedstocks are commercially available at reasonable prices (e.g., BASF's Ultrafuse, Nanoe's Zetamix), and can be also printed by the customer and then sent for heat treatment to the producer. Moreover, complete systems for component production with this technique are commercially available, such as Markforged's Metal-X and Desktop Metal's Studio 2 systems. These systems offer an optimized production cycle that maximizes the potential of this technique, minimizing porosity and defects during printing and deformations of sintered parts, all at equipment costs around €100k, which is less than 1/5 of the typical cost of a commercial LPBF system.

Overall, MEAM for soft ferromagnetic materials presents a low TRL and very limited Literature is available.[25–27] Despite insights gained from works on other MEAM or metal injection moulding metallic materials regarding feedstock creation, debinding, and sintering processes, the relationship between the properties of the starting material, process parameters, and magnetic properties of SFMs obtained via MEAM remains uncertain, necessitating further studies. However, despite its lower TRL and printing resolution compared to more established techniques, MEAM-MFF has been identified as an ideal technique to begin exploring additive manufacturing of SFMs for Hall thrusters. The objective of this work is to develop an economical, rapid, and fully controllable production process, capable of producing SFM components with the highest possible resolution and magnetic performance, without necessarily aiming for flight-ready models in this phase. To embark on this endeavour, an investment of approximately 17k€ was required, covering the purchase of an Fused Filament Fabrication (FFF) printer, an ultrasonic bath for debinding, and a tubular furnace for sintering with controlled atmosphere, along with consumables such as debinding solvents and inert gases for sintering treatment. A significant portion of the investment was allocated to the furnace, which can reach temperatures of 1600 °C, necessary for sintering technical ceramics, also under investigation alongside ferromagnetic materials.[28] With a lower-temperature furnace, costs can be reduced significantly.

Soft iron was chosen as the material for these preliminary investigations. As mentioned in Section I, soft iron ranks second only to iron-cobalt alloys in terms of saturation magnetization (2.16 T for Fe, 2.45 T for Fe50%Co[9]) and Curie temperature (770 °C for Fe,[9] 940 °C for 49%Fe49%Co2%V[11]). It also exhibits good coercivity (as low as 4 A/m) and high maximum relative permeability (up to 180,000). Additionally, it is economical compared to other soft ferromagnetic materials, making it an ideal benchmark for developing the production methodology. During the test campaign, a low-cost commercial filament was initially used, followed by the development of a customized filament in collaboration with an external company.

In the following, the results achieved to date in the definition of the production process are shown and the magnetic performances attained with the material tested are discussed. Further details will be found in forthcoming articles.

B. Materials and Method

1. Feedstock

The first feedstock analyzed was *pure iron Filamet*™ manufactured by The Virtual Foundry Inc.,[29] hereinafter referred to as TVF-PI. This filament comprises a binder system primarily composed of Polylactic Acid (PLA) with traces of a proprietary binding additive.[30] The metal particles within the filament are atomized iron particles with a reported purity exceeding 98 wt.%, with an unspecified dimension distribution and shape. Despite the name pure iron, the material is more accurately classified as low-carbon steel based on the previously provided definitions. For experimentation, a 500 g filament spool was used, with a reported metal content of 81.7 wt.% and a diameter of 1.75 ± 0.05 mm. The binder in this case must be removed through thermal treatment by submerging the part in a wicking agent. This powder extracts the binder by capillarity during the thermal process while maintaining the component's shape.[31,32] The powder recommended by the filament manufacturer (Sintering Ballast[33]), composed mostly of alumina (69-75 wt.%) and graphite (15-25 wt.%), was used for this purpose.

Based on the results obtained with the first filament, a new filament, referred to as NaMEX-Fe from here on, was created in collaboration with Nadir Srl.[34] This new filament represents an improvement over the previous one in all respects. It consists of a proprietary bicomponent binder with a metallic mass content of 90.2 wt.%. (51.3 vol.%). The binder includes a soluble component (4.9 wt.%) removable by immersion in cyclohexane, with the remainder being removed through thermal debinding. The metal particles have a D90 of 41.3 um, an apparent density of 3.65 g/cm^3, and a purity greater than 99.65% with a carbon content of 70 ppm, thus classifying it as soft iron. Also in this case the filament has a diameter of 1.75 ± 0.05 mm.

An image of the spools of both filaments is shown in Figure 5. Before the experimental campaign, each filament underwent thermogravimetric analysis, and differential scanning calorimetry. Additionally, the cross-sections of the filaments were examined using scanning electron microscopy (SEM)

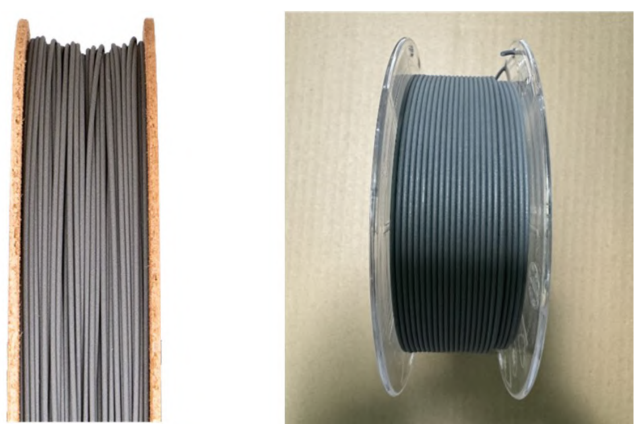

Figure 5. The Virtual Foundry's iron filament (left) and NaMEX-Fe filament (right).

2. Printing Parameters Optimization Campaign

For each material, to determine optimal printing parameters for minimizing process-induced porosities, multiple $25{\times}5{\times}5$ mm^3 cuboids with a central indentation were printed. All prints were conducted using the Ultimaker Cura 5.5 slicing software and a low-cost desktop printer (Mingda Magician X2), equipped with a direct drive extruder, a 0.6 mm hardened steel nozzle (E3D's v6), and a detachable PEI building plate. Variations in extruder temperature, line width, flow multiplier, and printing speed were explored within the ranges specified in Table 2. This table also outlines the primary parameters held constant across all prints, with all other settings matching the *standard quality* printing profile of the slicer software. Subsequently, each cuboid was transversely fractured along the indentation section and examined under an optical microscope to qualitatively assess porosity level. This iterative process continued until a satisfactory minimal porosity was achieved.

Table 2. Printing Parameters

Varied Parameters (Range)	
Extruder Temperature	190 - 220 °C
Line Width	0.6 - 0.8 mm
Flow Multiplier	75 - 125 %
Printing Speed	5 - 20 mm/s
Fixed Parameters	
Nozzle Diameter	0.6 mm
Layer Height	0.2 mm
Bottom Layers	9999
Bottom Infill Density	100%
Top/Bottom Pattern	Linear
Bed Temperature	30 °C (TVF-PI), 85 °C (NaMEX-Fe)
Enable Retraction	Off (TVF-PI), On (NaMEX-Fe)
Enable Print Cooling	Off
Combing Mode	All
Travel Speed	300 mm/s
Build Plate Adhesion Type	Skirt (1x3)
Initial Layer Horizontal Expansion	0.1 mm
Alternate Wall Directions	Enabled

3. Debiding and Sintering Campaign

To evaluate the feasibility of the production process and characterize the magnetic properties of materials under varying process parameters, toroids featuring square or circular cross-sections were printed with the optimized printing parameters with each material, then debound and sintered. The superior printability of the NaMEX-Fe filament also allowed for the creation of geometric feature testers. The thermal treatments applied to the specimens aimed to assess the influence of the working atmosphere and temperature on densification, shape retention, and magnetic properties.

For the TVF-PI filament, a total of 9 specimens, mostly comprising pairs of circular and square cross-section toroids, underwent debiding and sintering in 5 different thermal treatments with 4 distinct thermal profiles (SP1, SP2, SP3, SP2-VAC), as outlined in Figure 6, all with a sintering time of 6 hours. The toroids were debound using a one-step thermal process carried out either in air in a Metal 3D Printing Starter kiln by Sapphire 3D or under vacuum (<50 mbar) in a Nanoe's Zetasinter tubular furnace. In all treatments, the green parts were placed in an alumina crucible and submerged in a wicking agent. Some of the debound toroids were removed from the crucible, cleaned with a brush to remove the wicking agent, and then weighed, measured, and, in some cases, fractured to observe their cross-sections. Sintering was carried out entirely in the low vacuum tubular furnace or with 99.999% pure Argon. In the latter case, the gas flow was regulated using an analogic flowmeter, while the pressure in the furnace was maintained at the atmospheric value using a bubbler filled with distilled water, connected to the downstream end of the furnace.

The characterization campaign of the NaMEX-Fe filament is still ongoing, and so far, only 3 toroids and one geometric tester have been processed. The components underwent two baths in cyclohexane at 60°C for a total of 36 hours reaching 70 wt.% of removal of the soluble binder. Subsequently, thermal debinding and sintering were carried out again in the Zetasinter tubular furnace using an Argon-2%H2 atmosphere at a flow rate of 0.5 l/min throughout the treatment, following the cycle indicated in Figure 6.

To measure the magnetic properties of the prepared samples, an inductive method was employed with the toroidal specimen. Using a primary coil wrapped around the specimen, a time-varying current $i(t)$ was circulated. Thus, the magnetic field strength was calculated using Ampere's law as $H(t) = \frac{N_1 i(t)}{\pi D_m}$, where

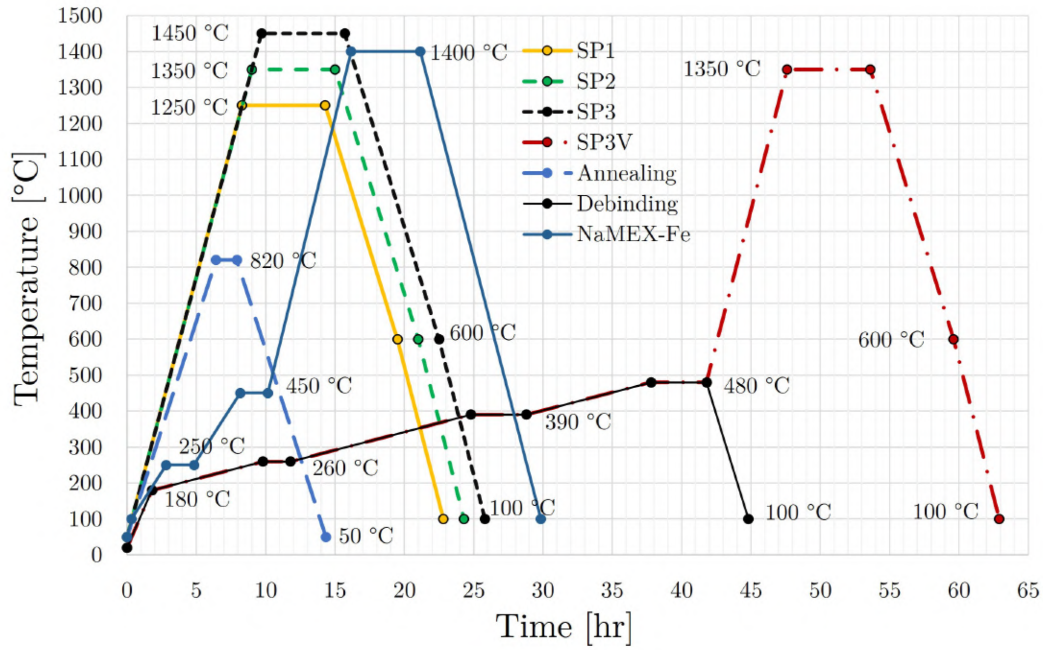

Figure 6. Debiding, sintering and annealing treatments time-temperature curves.

D_m is the average diameter of the specimen, and N_1 is the number of turns of the coil. A secondary coil consisting of N_2 turns was wound around the specimen to measure the induced voltage V_2. The magnetic flux density was then calculated through Faraday's law as $B(t) = \frac{\int_0^t V_2 dt}{N_2 A}$, where A is the cross-sectional area of the specimen. By analyzing the B-H loop for each sample, we estimated the magnetic flux density saturation and coercivity as $B_M = B|_{\max(H)}$ and $H_C = H|_{B=0}$, respectively. All tests were conducted at a constant temperature of $0°C$ using a deionized water-ice bath. Each specimen was previously coated with three layers of non-magnetic, corrosion-resistant enamel to prevent chemical interaction between the sample material and the environment.

As a reference material, an ARMCO pure iron sample was utilized to evaluate the parameters $B_{M,0}$ and $H_{c,0}$, i.e., the magnetization saturation and the coercivity of the ARMCO sample. This reference sample was manufactured by cutting a round bar to form a ϕ 42 mm × 16 mm cylinder, further drilling a central hole with a diameter of 21 mm to achieve a toroidal-shaped sample. The results were also compared with data obtained from Literature sources for ARMCO iron.[35]

C. Results

1. Feedstock and Printed Parts

The TVF-PI filament was problematic during printing due to its fragility, which often led to breakages near both the extruder motor and the spool, as well as frequent partial clogging near the nozzle from segregation phenomena. To address these issues, it was necessary to feed the printer with straight portions of filament approximately 1 meter in length, previously separated from the spool and heated to 60°C for reshaping. In case of clogs or filament breakage, the printing process was repeated. These problems were completely resolved with the second filament, which exhibited excellent printability. Figure 7 shows some green parts printed with both filaments.

Figure 8 presents an SEM image of the cross-section of the TVF-PI filament compared to a commercial MFF-MEAM filament with a metal content similar to the NaMEX-Fe filament. It can be observed that the metal particles exhibit a homogeneous distribution within the TVF-PI filament section but have an irregular and agglomerated shape and occupy a small portion of the cross-section. The calculated average volumetric

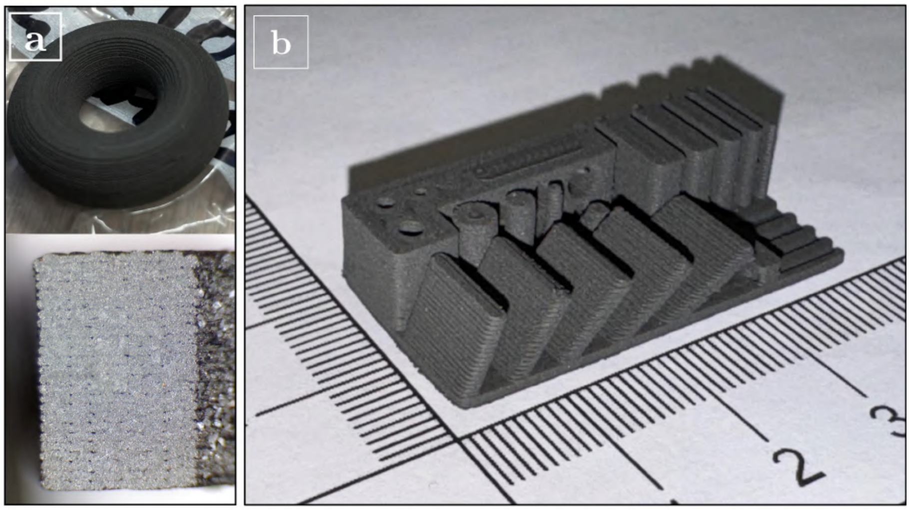

Figure 7. Green components printed with TVF-PI (a) and NaMEX-Fe (b).

density of the metal particles is about 30%, while that extrapolated through the analysis of two different SEM cross-sections with ImageJ (and assuming a uniform distribution of particles along the filament) is 10-13%. This loading is considerably lower than those reported in the Literature for metal MEAM materials, which typically range from 50-75%[23, 36] and compared to that of the NaMEX-Fe filament (50%).

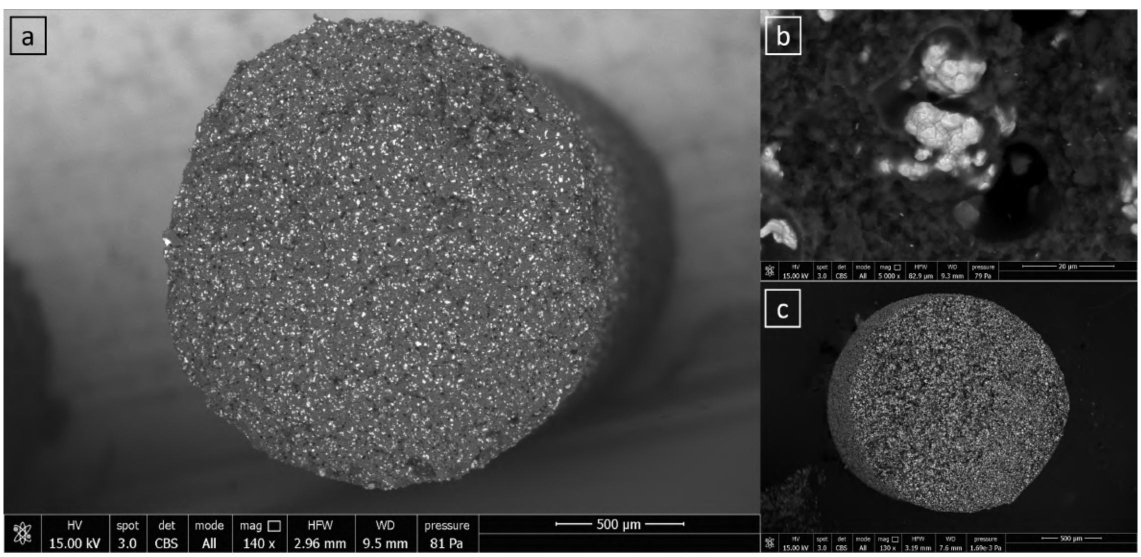

Figure 8. SEM image of the cross-section of the TVF-PI filament (a), a magnified view of an iron particle (b), and the cross-section of a commercially available stainless steel filament for comparison (c).[37]

2. Debiding and sintering

Figure 9a depicts cross-sectional photos of some debound TVF-PI specimens. Large cavities are observed along the lateral interface between the raster lines. Additionally, with reference to Figure 7a, it is evident that the cavities between the raster lines formed during printing have significantly expanded compared to those present in the green part. The internal cavities observed in the cross-sectional analysis of the debound samples are most likely caused by a combination of phenomena involving the pressure buildup from the decomposing binder and the kinetics of the capillary extraction of the primary binder: internally, the binder begins to degrade before the surrounding material is extracted. To address this issue, most high-performance MEAM materials, including NaMEX-Fe, employ a two-step debinding process (solvent/catalytic and thermal).[38] One solution used in the Literature to mitigate this phenomenon is to significantly prolong the duration of

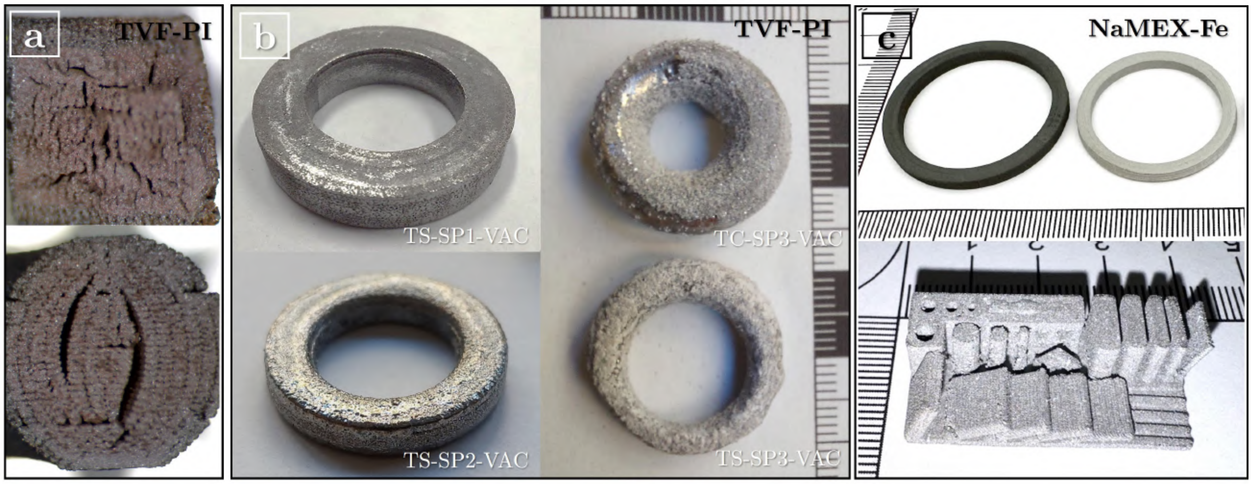

Figure 9. Cross section view of some debound TVF-PI specimens (a). Photo of some of the sintered TVF-PI toroids (b) and NaMEX-Fe (c) specimens.

the thermal treatment, reducing the heating rate during heating ramps,[31,39] although this makes the process costly or impractical in many cases. The other problem that likely contributed to cavity formation is again the low volumetric powder loading of the metal particles.

Ultimately, these voids represent one of the major issues for the mechanical and magnetic properties of the analyzed feedstock. Defects such as voids and cracks can impede and hinder the motion of magnetic domain walls. As a result, more energy is required to magnetize or demagnetize the material, degrading its permeability. Figure 10 shows the cross-section of some of the TVF-PI specimens, highlighting the presence of macro-voids in almost all specimens except those sintered at 1450 °C, which are partially fused, as seen in Figure 9b. In contrast, the NaMEX-Fe specimens exhibited excellent shape retention even with sintering at 1400 °C, as shown in Figure 9b.

The superior performance of the NaMEX-Fe material is also confirmed by density measurements performed using the Archimedes method, which indicated a density of 92% of that of iron. In contrast, the TVF-PI specimens showed a variable density from 57.4% to 90.2%, exhibiting a linear trend with temperature. For NaMEX-Fe, the shrinkage was almost 15% isotropic, while for TVF-PI, shrinkage also varied linearly with temperature, particularly pronounced for sample height, reaching 35%, whereas diameter variation levelled around 12%.

The reason for the better performance of NaMEX-Fe is probably its higher volumetric powder loading. It has been widely demonstrated for both metal MEAM and MIM that a higher volumetric loading allows for a reduction in the porosity of final parts and helps maintain the original shape of the component.[23,36,38] Therefore, it is not surprising that phenomena such as shape loss and anisotropic shrinkage were encountered with TVF-PI.

3. Magnetic Properties of the Sintered Specimen

The graphs in Figure 11 show the hysteresis curves for all the specimens analyzed. The graphs also include curves for the benchmark toroid and a reference ARMCO iron.[35]

Regarding the TVF-PI material, the first graph (Figure 11a) depicts specimens subjected to debinding in air and sintering in vacuum at different temperatures. It is noted, in particular, how the saturation magnetization increases almost linearly with the sintering temperature, reaching up to approximately 98% of that of the pure iron reference for the cycle at 1450°C, although partial melting of the specimen was observed in this case. The coercivity of all three specimens is comparable to that of the benchmark specimen and about 50% lower than the reference pure iron.

The graph (Figure 11b) shows the curves of the specimen that underwent the entire treatment in vacuum and those sintered in Argon. It is observed that the specimen debound in vacuum has a saturation magnetization and coercivity approximately 30% higher than those of the specimen with debinding in air (TS-SP2-VAC). The specimens sintered in Argon show very similar curves, demonstrating a certain repeatability in the manufacturing process. However, the magnetic properties in this case are lower compared to

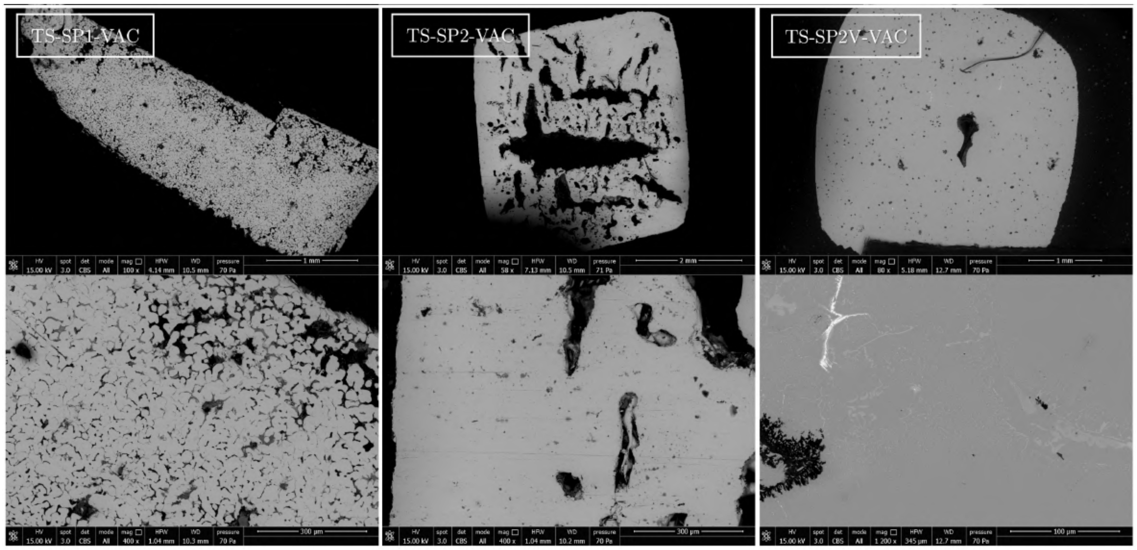

Figure 10. Cross section of polished TVF-PI specimens exhibiting large macro-voids.

the TS-SP2-VAC specimen with a variation of saturation magnetization ranging from 52-61% with respect to TS-SP2-VAC, and a coercivity with oscillation of about 20%.

Lastly, Figure 11c shows the effect of annealing on the magnetic properties. For all specimens except the one sintered at 1450 °C, a reduction in coercivity of 30-60% is observed, while the saturation magnetization also increases by 2-10%. The reduction in coercivity is especially prominent for the specimen debound in vacuum.

The NaMEX-Fe material has been characterized only preliminarily, and Figure 11d shows the BH curve obtained for one of the sintered toroids described previously. The NaMEX-Fe toroid demonstrated better magnetic properties than the previous material, excluding from comparison the toroids that showed significant shape variation or melting. In particular, the toroid achieved magnetic properties comparable to those of the benchmark toroid, although still inferior to the maximum properties of the pure iron reference.

D. Discussion and Final Considerations

In summary, the TVF-PI filament served as a valuable learning experience despite its unsatisfactory results, paving the way for the development of the NaMEX-Fe filament, which performed remarkably well as a first iteration. NaMEX-Fe sintered components achieved relative density exceeding 92%, a saturation magnetic field greater than 60% and a lower coercitivity with respect to pure iron, and excellent dimensional stability.

The current experimental campaign aims to identify process parameters that can enhance both the material's density and magnetic properties, which are directly related. Higher sintering temperatures and increased gas flow are expected to bring improvements. Further enhancements could be achieved through annealing cycles, which have shown the ability to increase the saturation magnetic field by up to 10% and significantly reduce coercivity for TVF-PI samples.

Current critical challenges of the technique include deformation during sintering and low resolution. Advanced commercial production systems offer software for predicting and compensating for these deformations, although free versions of such software are currently unavailable. Regarding resolution, efforts will include testing smaller nozzles (down to 0.2 mm), even if, as nozzle size decreases, the particle size of the starting powder becomes crucial, probably requiring finer powders with respect to the one used for very small nozzles. Additionally, the mechanical properties of components remain to be evaluated, a task planned in the near future.

Mid-term plans involve a second iteration of the NaMEX-Fe filament, aiming to maximize volumetric powder loading (ideally exceeding 60%) and utilizing higher quality powders. This approach aims at minimizing component deformation issues and maximising part densification.

Regarding other materials, during the development of the NaMEX-Fe filament, Nadir Srl also provided us with a copper powder pellet feedstock (NaMEX-Cu). Figure 12 shows green and sintered copper components.

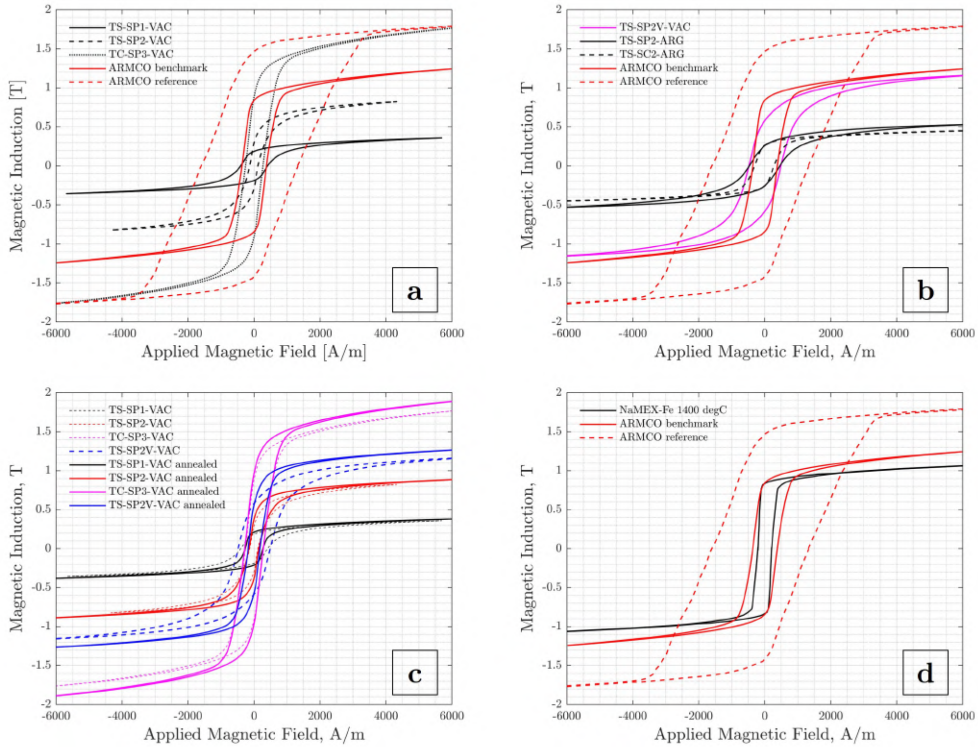

Figure 11. BH curves depicting TVF-PI specimens under varied treatments: (a) debound in air, (b) debound and sintered in vacuum, and debound in air and sintered in argon, (c) and post-annealing. BH curve for a NaMEX-Fe toroid (d).

The latter present $> 90\%$ of relative density and good shape retention confirming the technique's versatility with multiple materials. Short-term plans include developing a filament using a 50%Fe 50%Co alloy, for which the powders have already been procured.

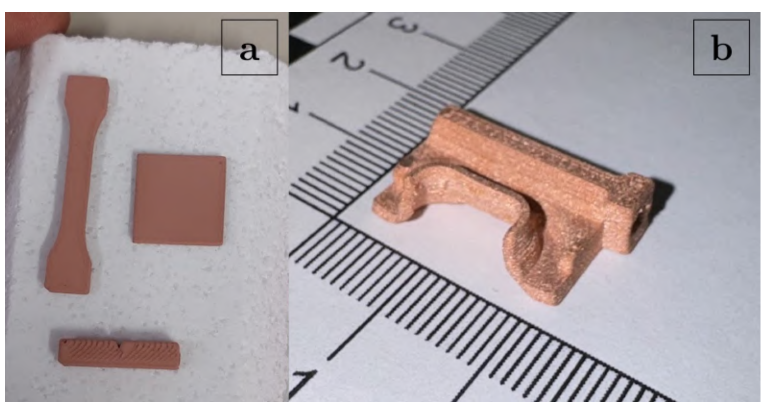

Figure 12. Green copper parts (a), and complex geometry copper component after sintering (b).

III. Case Study: Additively Manufactured Magnetic Circuit for a 300 W Hall Thruster

A. Introduction

To test the actual capabilities of the manufacturing technique described in the previous section, we used it to create a prototype magnetic shielding circuit for a low-power Hall thruster. The original goal was to take the magnetic circuit of an existing low-power thruster and modify its design for additive manufacturing. Unfortunately, the Literature provides very few details about low-power thrusters, particularly those with a magnetic circuit sized appropriately for sintering in the UniPi's furnace (<80 mm). Therefore, it was decided to design a thruster from scratch using the scaling methodology developed at the University of Pisa,[40] which has been successfully used to design the 20 kW dual-channel magnetically shielded TANDEM thruster.[41]

After defining the geometric dimensions of the discharge channel using this scaling methodology, the detailed geometry of the entire thruster was determined through successive iterations with magnetic and thermal simulations in Comsol Multiphysics. The designed magnetic circuit consists of three components (to allow for the insertion of coils) and can generate a magnetically shielded topology with a radial magnetic field peak in the center of the channel up to 200 G. Additionally, the circuit features an integrated propellant distribution system and a complex geometry that minimizes material usage maintaining a stiff structure.

The designed circuit was printed using NaMEX-Fe filament and sintered according to the previously described procedure. The sintered circuit was then assembled, and the difference from the designed magnetic field was measured using a specially designed magnetic field mapper.

B. Prototype Design

The first step was to determine the dimensions of the discharge channel to achieve an anode efficiency greater than 40% with a power output below 500 W. Figure 13 shows graphs obtained by applying the scaling methodology, illustrating the anode thrust efficiency as a function of nominal power and channel width for an average diameter of 35 mm. These graphs include scenarios with plasma density equal to the reference thruster, increased by 50%, and with a peak radial magnetic field of 200 G.

Since the total efficiency increases less significantly with increasing power, a nominal power of 300 W was chosen. The channel height was selected to be 8 mm as a compromise between maximizing anode efficiency and providing sufficient space for the internal magnetic circuit, also allowing room for an internal cathode. The nominal operating parameters of the scaled thruster, referred to hereinafter as MExT-300, are indicated in Table B.

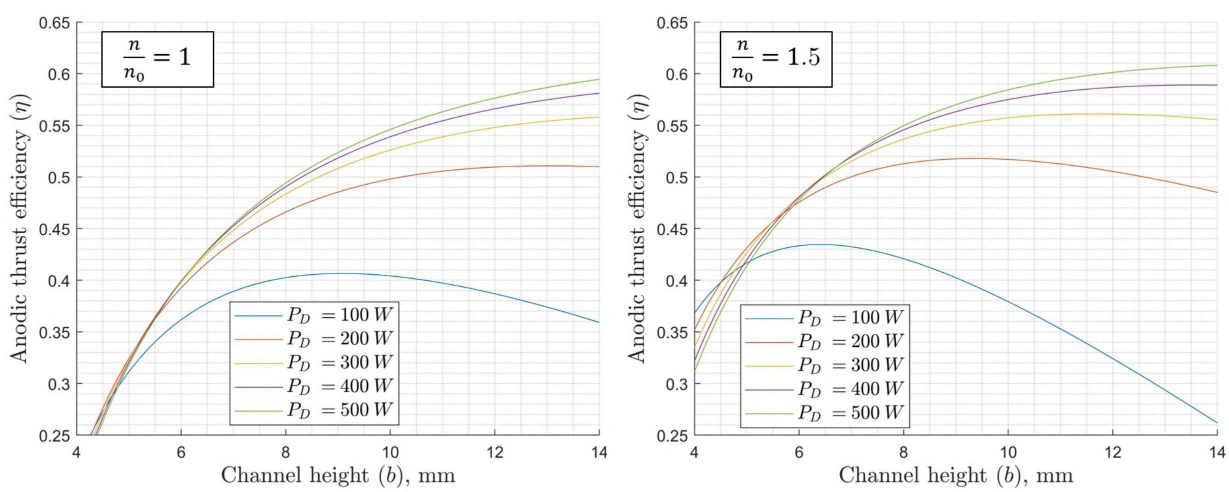

Figure 13. Plots obtained with the scaling methodology for a thruster of 35 mm of mean diameter, showing the trend of anodic thrust efficiency with channel height for different discharge powers. The plot on the left is for a thruster scaled with the same characteristic plasma density of the reference one, whereas the one on the right assumes an increase of 50% in plasma density.

Table 3. Nominal Operating Characteristics of the MExT-300.

Geometry	
Channel mean diameter, d [mm]	35.0
Channel height, b [mm]	9.00
Channel length, L [mm]	15.0
Operative parameters	
Nominal discharge power, P_D [W]	300
Peak radial magnetic field, B_r [G]	200
Discharge voltage, V_D [V]	170
Anodic mass flow rate, [mg/s]	1.62
Expected performance	
Thrust, T, [mN]	22.9
Anodic thrust efficiency, η_T [%]	54
Anodic specific impulse, I_{sp} [s]	1430
Power loss to walls [W]	63.3
Power loss to anode [W]	8.70

The next step was to define the preliminary characteristic of the magnetic circuit to meet the following requirements:

- A peak radial magnetic field of at least 200 G at the channel median line without saturation throughout the magnetic circuit ($B_{\max} < 0.8\ B_{\text{saturation}}$)
- Fully magnetically shielded topology
- Minimum wall thickness of 1 mm (to ensure at least two raster prints for features, as thinner features could show significant deformation during sintering)
- Use of coils with mineral-insulated cables

Iterative simulations were conducted in Comsol Multiphysics using the magnetic field module and incorporating the BH curve of the material shown in Figure 11 for the magnetic circuit material, scaled by 150% to account for the expected magnetic performance increase obtainable with high-temperature sintering and annealing. Figure 14 illustrates the magnetic flux streamline lines for the defined preliminary geometry and the magnetic field at the channel median line. AWG 24 wires were chosen for the coils, and the number of windings for the outer and trim coils was selected to allow all coils to operate with the same current of 4.5 A.

The geometry of the circuit was designed to be fabricated in three parts to facilitate the insertion of coils during assembly. Additionally, space was reserved for integrating a copper thermal dissipation system, which allows heat to be transferred away from the internal region of the thruster and radiated into the environment. Preliminary 2D thermal simulations using Comsol Multiphysics with modules for solid heat transfer, surface-to-surface radiation, and electromagnetic heating confirmed the effectiveness of this approach. With a simple design, it was possible to lower the internal inner pole temperature by over 50°C, as shown in Figure 15. In the simulation, the thermal load from the coil was automatically calculated with the electromagnetic heating multiphysics module, whereas the thermal load from the plasma were estimated conservatively to be twice the one calculated with the scaling procedure and shown in table B.

After defining the preliminary geometry, 3D simulations were conducted to assess the impact of material removal, such as through openings and holes, on the magnetic field. The simulations showed that the introduced lightening features and cavities cause variations in the radial magnetic field at the channel centre of less than 1% and are therefore feasible.

Subsequent 3D thermal simulations were conducted to re-evaluate the effect of these cavities and determine the design of the copper thermal dissipation system. Following a series of iterations, a final geometry

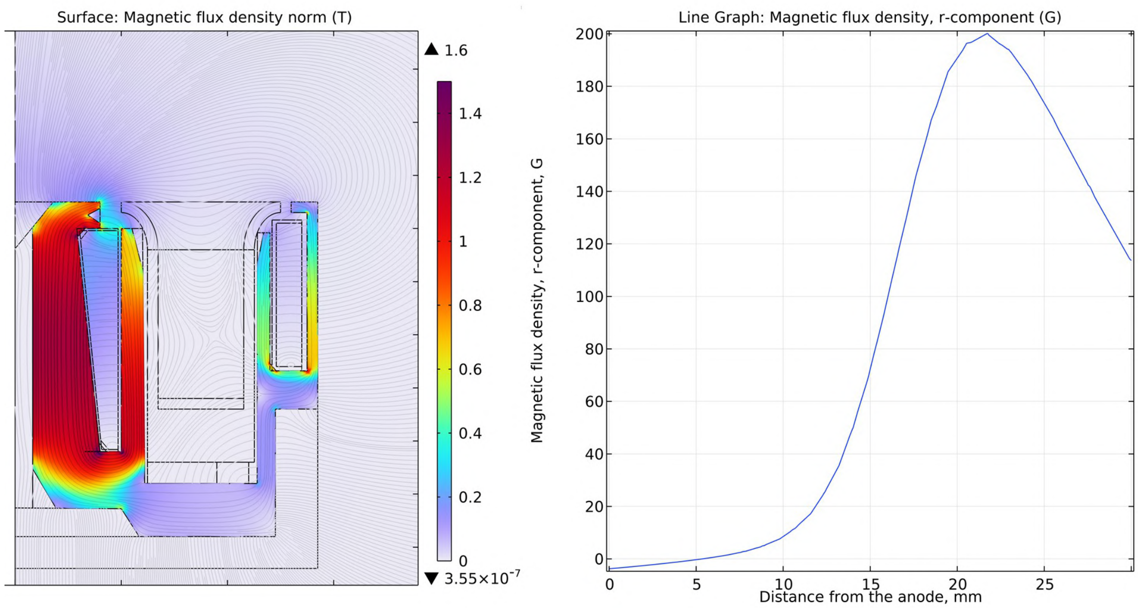

Figure 14. Magnetic flux streamlines and magnetic flux density surface plot showing a full magnetically shielded configuration without saturation (left). Radial magnetic flux density component along the median line of the channel (right).

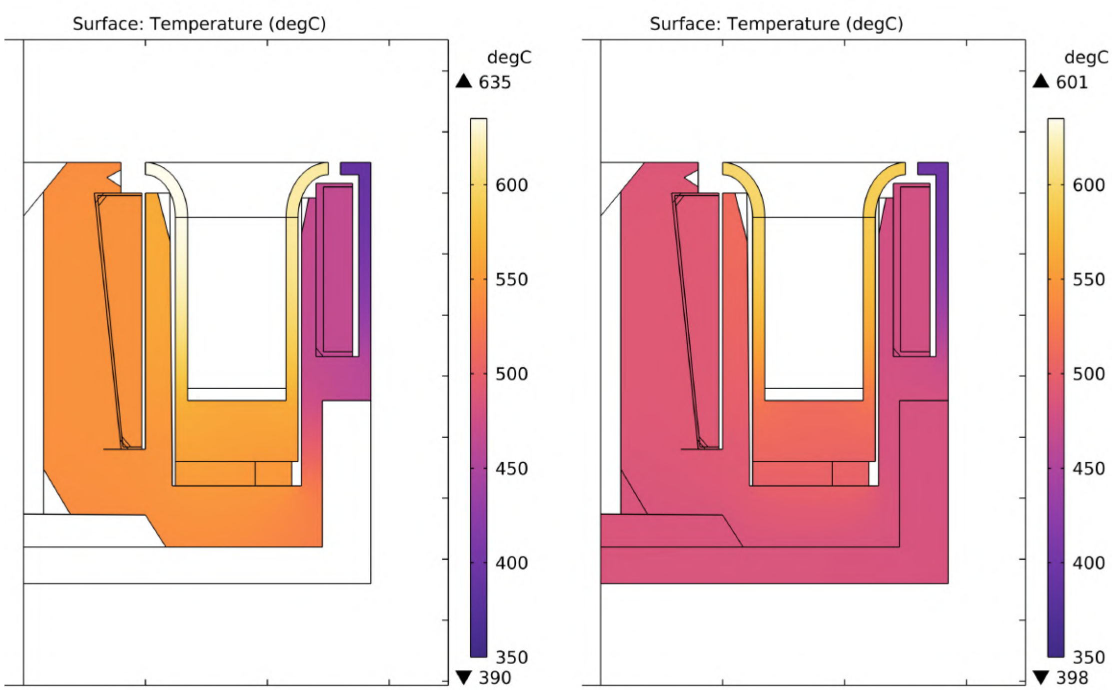

Figure 15. Temperature distribution comparison in the thruster: without the copper component (left) and with the copper thermal dissipation system integrated (right).

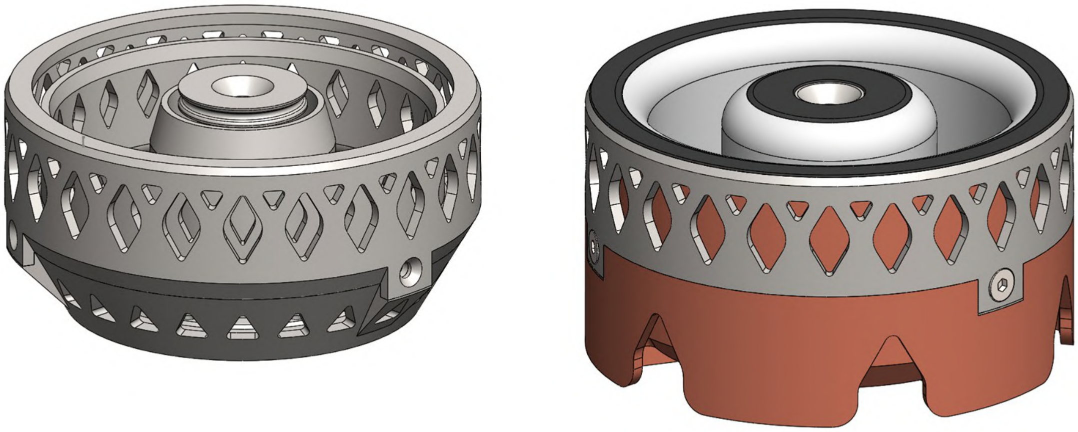

Figure 16. MExT-300 magnetic circuit (left) and assembly (right).

for the circuit and its components was defined. Additionally, holes were introduced for coil wires, fluid connections, and links between various components. The final design of the magnetic circuit and the thruster is depicted in Figure 16.

The thruster also features an integrated gas distribution system, significantly reducing the size of the anode, which in this design is implemented as a simple annular plate at the bottom of the channel. The channel itself is designed for additive manufacturing and will be printed in alumina with MEAM following the procedure defined in the companion paper presented at the conference.[28] The thermal dissipation system was designed using topology optimization techniques and is also intended to be printed using MFF-MEAM with the available copper feedstock at UniPi.

C. Prototype Manufacturing

In Figure 17, the various parts of the magnetic circuit are shown in the slicing software. Note that the components were scaled up in the slicing software to accommodate shrinkage and a brim was implemented to improve adhesion to the build plate. All circuit parts were successfully printed in a total of approximately 6 hours without significant defects, aside from slight fragmentation of the raster near the walls due to filament viscosity. Subsequently, the circuit underwent the previously described heat treatment, achieving excellent final quality. Figure 18 depicts the printed and sintered circuit. The outer ring experienced slight base deformation, complicating assembly slightly, but overall, the circuit retained its original shape well and is free from oxidation.

In the short term, the circuit's magnetic field will be mapped using a magnetic field mapper developed at the University of Pisa, previously used to map the magnetic field of the TANDEM thruster.[42] The mapping

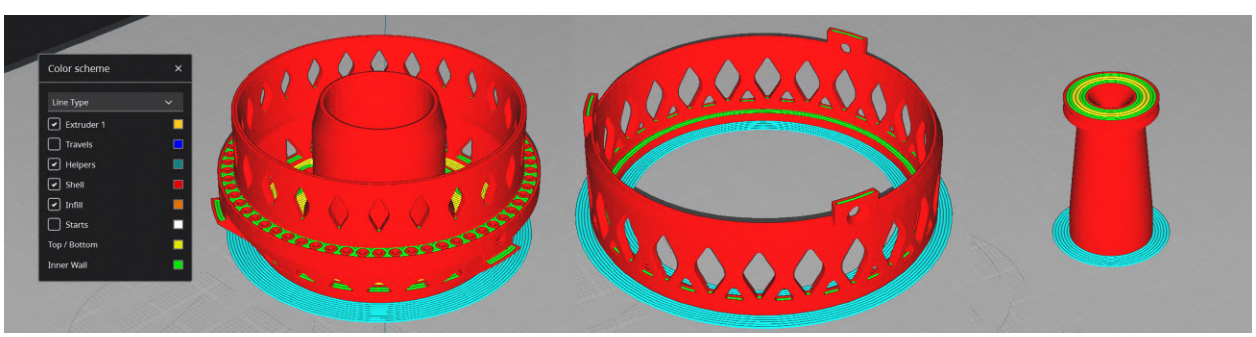

Figure 17. MExT-300 magnetic circuit component sliced in Cura.

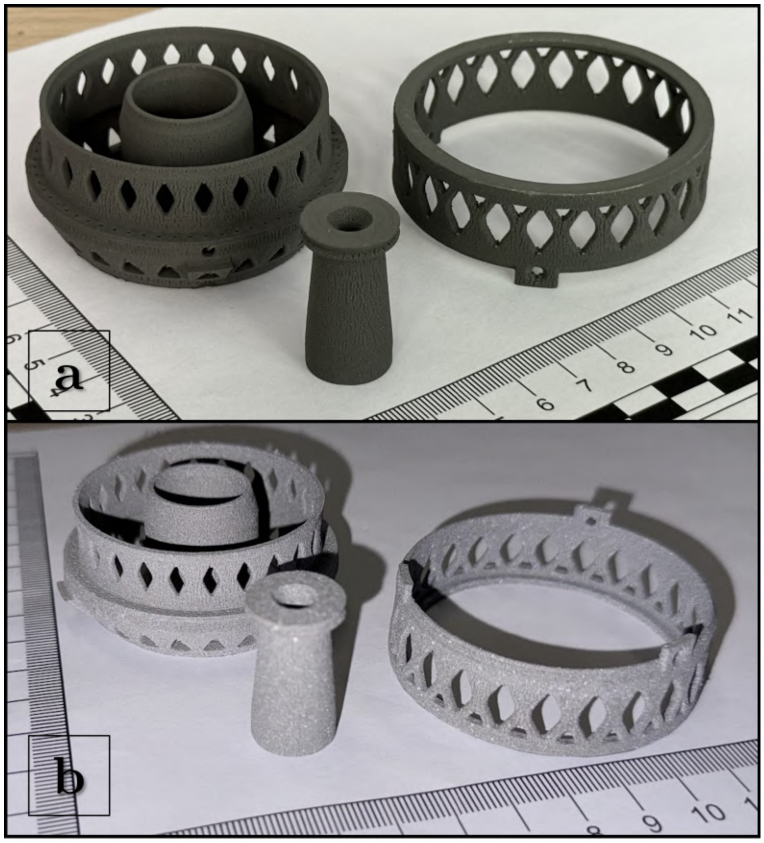

Figure 18. MExT-300 as printed (a) and as sintered (b).

head is designed to be compatible with various types of 3D printers; thus, a different printer with a smaller print bed will be used compared to previous tests. The magnetic mapper and the specially developed 3D Helmholtz coil used for calibration are shown in Figure 17.

Many of these modifications could have been achieved using traditional techniques, albeit with greater complexity and longer lead times. Nevertheless, the circuit was completed in less than two days, with only a few hours of more intense process monitoring and at a reasonable cost. No adjustments were made using traditional manufacturing techniques on the prototype. The mapping process will be used to verify the component's functionality, with no significant deviations expected from simulations.

IV. Conclusion

This study represents an initial exploration into additive manufacturing of ferromagnetic components for electric propulsion. It aims to generate interest in the numerous design opportunities offered by additive manufacturing, both for enhancing existing thrusters and developing novel concepts. The AM methodology outlined in this paper marks one of the first feasibility demonstrations in the Literature for producing Hall thruster magnetic circuits using AM techniques. While a few other companies and authors have also prototyped MC circuits using different AM methods, the proposed MEAM-based approach emerges as a viable and cost-effective alternative accessible to many small laboratories and companies.

The tested material demonstrated good printability, enabling the production of parts with complex geometries, achieving a sintered relative density of 92%, saturation magnetization of approximately 60%, and lower coercivity compared to reference pure iron. The printing of the magnetic circuit for the MExT-300 thruster showcased the technique's potential. A mapping of the magnetic field generated by the circuit will soon be conducted to verify its functional effectiveness. Some concerns remain regarding repeatability and achievable tolerances with this process, but ultimately, this work represents a significant initial stride toward a new generation of highly optimized and efficient Hall thrusters.

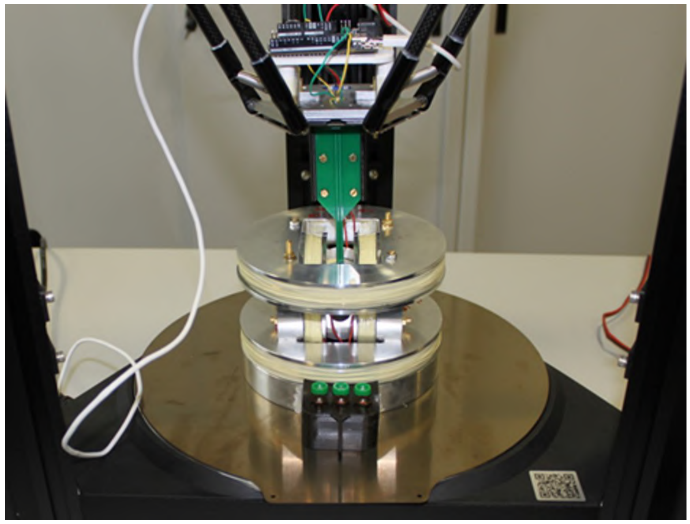

Figure 19. Magnetic field mapper head and tri-axial Helmholtz coil used for its calibration.

Acknowledgments

We want to express our heartfelt gratitude to Professor Mariano Andrenucci for his invaluable contribution to our professional and personal development.

We would also like to thank Andrea Brunetin (brunetin@nadir-tech.it) and Paolo Scopece (scopece@nadir-tech.it) of Nadir Srl for their availability and the incredible work they did in creating the NaMEX-Fe filament, and Gianluca Caposciutti (gianluca.caposciutti@unipi.it) for his fantastic work with magnetic hysteresis curve measurements.

References

[1] Noah Zachary Warner. Theoretical and experimental investigation of hall thruster miniaturization, June 2007.

[2] M. El Idrissi. Development of new high temperature wires and cables for space applications. In *Space Passive Component Days, 1st International Symposium*, 2013.

[3] Ludovico Lorello, Igor Levchenko, Kateryna Bazaka, Michael Keidar, Luxiang Xu, S. Huang, J. W. M. Lim, and Shuyan Xu. Hall thrusters with permanent magnets: Current solutions and perspectives. *IEEE Transactions on Plasma Science*, 46(2):239–251, 2018.

[4] G. B. Popkov V. K. Kharchevnikov A. I. Bugrova, A. I. Morozov. Investigation of plasma lens characteristics. *Zhurnal Tekhnicheskoi Fiziki*, 56(2):307–311, 1986.

[5] Dan M Goebel, Richard R Hofer, Ioannis G Mikellides, and Ira Katz. Conducting wall hall thrusters. In *49th AIAA/ASME/SAE/ASEE Joint Propulsion Conference*, Reston, Virginia, July 2013. American Institute of Aeronautics and Astronautics.

[6] Standard specification for magnetic pure iron. American Society for Testing and Materials International (ASTM), 2023. A112623.

[7] Standard specification for soft magnetic iron parts fabricated by powder metallurgy techniques. American Society for Testing and Materials International (ASTM), 2022. A81115(2022).

[8] Standard specification for low-carbon magnetic iron. American Society for Testing and Materials International (ASTM), 2017. A84817.

[9] David Jiles. *Introduction to Magnetism and Magnetic Materials (3rd ed.)*. CRC Press, Boca Raton, 2015.

[10] AK Steel Holdings Corporation. *ARMCO Pure Iron Datasheet*, 2021. Accessed: (06/04/2024).

[11] Carpenter technology. *Hiperco 50 datasheet*, 2020. Accessed: (06/04/2024).

[12] Additive manufacturing — general principles — fundamentals and vocabulary. International Organization for Standardization (ISO) and American Society for Testing and Materials International (ASTM), 2021. ISO/ASTM 52900:2021.

[13] Ana Vafadar, Ferdinando Guzzomi, Alexander Rassau, and Kevin Hayward. Advances in metal additive manufacturing: A review of common processes, industrial applications, and current challenges. *Applied Sciences*, 11(3), 2021.

[14] Paul R. Gradl, Sandy E. Greene, Christopher Protz, Brad Bullard, James Buzzell, Chance Garcia, Jessica Wood, Robin Osborne, James Hulka, and Kenneth G. Cooper. *Additive Manufacturing of Liquid Rocket Engine Combustion Devices: A Summary of Process Developments and Hot-Fire Testing Results*.

[15] Bryan Ramiro Rodriguez-Vargas, Giulia Stornelli, Paolo Folgarait, Maria Rita Ridolfi, Argelia Fabiola Miranda Pérez,

and Andrea Di Schino. Recent advances in additive manufacturing of soft magnetic materials: A review. *Materials*, 16(16), 2023.

[16]V. Chaudhary, S.A. Mantri, R.V. Ramanujan, and R. Banerjee. Additive manufacturing of magnetic materials. *Progress in Materials Science*, 114:100688, 2020.

[17]Reilly S. W. Kerber T. V. Brooks J. W. Goebel D. M. Conversano, R. W. Development of and acceptance test preparations for the thruster component of the ascendant sub-kw transcelestial electric propulsion system (astraeus). In *36th International Electric Propulsion Conference*, 2019.

[18]Ryan W Conversano, Robert B Lobbia, Steven M Arestie, Alejandro Lopez-Ortega, Vernon H Chaplin, Sean W Reilly, and Dan M Goebel. Demonstration of one hundred kilogram xenon throughput by a low-power hall thruster. *J. Propuls. Power*, pages 1–15, October 2022.

[19]Samad A. FirdosyRobert and et. al. Magnetic elements and methods for the additive manufacture thereof, 2019. US20190366435A1.

[20]Samad Firdosy, Nicholas Ury, John Paul Borgonia, Bryan McEnerney, Ryan Conversano, Richard Hofer, Adam Hermann, Huseyin Ucar, Vilupanur A Ravi, and R Peter Dillon. Processing–microstructure–property relationships in a laser-deposited Fe-co-V alloy. *Adv. Eng. Mater.*, 24(4):2100931, April 2022.

[21]S. Firdosy and et. al. Poster: Advancing electric propulsion technology with 3d printing (adept3d). In *FY23 Topic Areas Research and Technology Development (TRTD)*, 2023.

[22]3d printing magnetic circuit components for hall effect thrusters. https://www.sbir.gov/sbirsearch/detail/1560093, 2018.

[23]Chanun Suwanpreecha and Anchalee Manonukul. A review on material extrusion additive manufacturing of metal and how it compares with metal injection moulding. *Metals*, 12(3), 2022.

[24]Joamin Gonzalez-Gutierrez, Santiago Cano, Stephan Schuschnigg, Christian Kukla, Janak Sapkota, and Clemens Holzer. Additive manufacturing of metallic and ceramic components by the material extrusion of highly-filled polymers: A review and future perspectives. *Materials*, 11(5), 2018.

[25]E. Carreño-Morelli, L. Meylan, M. Rodriguez-Arbaizar, X. Carthoblaz-Délèze, B. Sahli, R. Chandran, and G. Balestra. Solvent-on-granules 3d-printing and material extrusion of soft magnetic fe-6.5si alloy. In *Euro PM2023 Proceedings*, 2023.

[26]Vincent Martin, Frédéric Gillon, Denis Najjar, Abdelkader Benabou, Jean-François Witz, Michel Hecquet, Philippe Quaegebeur, Matthieu Meersdam, and Delphine Auzene. Mim-like additive manufacturing of fe3 *Journal of Magnetism and Magnetic Materials*, 564:170104, 2022.

[27]Yaozhong Zhang, Lucrezia Poli, Elias Garratt, Shanelle Foster, and Aljoscha Roch. Utilizing fused filament fabrication for printing iron cores for electrical devices. *3D Printing and Additive Manufacturing*, 7(6):279–287, 2020.

[28]G. Giammarinaro, F. Marconcini, C. Guidi, F. Tamburrino, M. M. Saravia, A. V. Razionale, F. Paganucci, and G. Becatti. Fused filament fabrication of alumina components for hall thrusters. In *38th International Electric Propulsion Conference Proceedings*, 2024.

[29]Inc. The Virtual Foundry. The virtual foundry's website. `https://thevirtualfoundry.com/`. Accessed: (06/04/2024).

[30]Inc. The Virtual Foundry. Pure iron filamet safety datasheet. `https://thevirtualfoundry.com/wp-content/uploads/2024/03/The-Virtual-Foundry-SDS-Pure-Iron-24-01.pdf`. Accessed: (06/04/2024).

[31]Randall M. German Ravi K. Enneti, Seong Jin Park and Sundar V. Atre. Review: Thermal debinding process in particulate materials processing. *Materials and Manufacturing Processes*, 27(2):103–118, 2012.

[32]Lovro Gorjan, Aleš Dakskobler, and Tomaž kosmač. Partial wick-debinding of low-pressure powder injection-moulded ceramic parts. *Journal of the European Ceramic Society*, 30(15):3013–3021, 2010.

[33]Inc. The Virtual Foundry. Sintering refractory ballast (steel blend) safety datasheet. Accessed: (06/04/2024).

[34]Nadir srl website. https://nadir-tech.it/, 2018.

[35]R. Principe. Low carbon steel for magnetic yokes. In *CERN seminar: Iron for magnet yokes*. European Organization for Nuclear Research (CERN), 2015.

[36]Heungseok Oh, Taehyeob Im, Jungsuk Pyo, Jai-Sung Lee, and Caroline Sunyong Lee. Study of solid loading of feedstock using trimodal iron powders for extrusion based additive manufacturing. *Sci. Rep.*, 13(1):4819, March 2023.

[37]Zetamix (by Nanoe). Aisi 316l filament webpage. `https://zetamix.fr/produit/filament-acier-inoxydable-316l/`. Accessed: (06/04/2024).

[38]Naveen Kumar Bankapalli, Vishal Gupta, Prateek Saxena, Ankur Bajpai, Christian Lahoda, and Julian Polte. Filament fabrication and subsequent additive manufacturing, debinding, and sintering for extrusion-based metal additive manufacturing and their applications: A review. *Composites Part B: Engineering*, 264:110915, 2023.

[39]F. Marconcini, F. Tamburrino, G. Giammarinaro, A. V. Razionale, and F. Paganucci. Investigation of the material extrusion additive manufacturing of an inconel-718 filament. In *Euro PM2023 Proceedings*, 2023.

[40]G. Giammarinaro, F. Marconcini, G. Becatti, M. M. Saravia, M. Andrenucci, and F. Paganucci. A scaling methodology for high-power magnetically shielded hall thrusters. *J. Elect. Propuls.*, 2, 2023.

[41]S. Scaranzin, F. Scortecci, E. Bonelli, Sestini. L., M. Bartali, F. Avanzi, U. Cesari, F. Dini, F. Cannelli, G. Giammarinaro, F. Marconcini, F. Paganucci, M. M. Saravia, G. Becatti, and D. Estublier. Characterisation of a 20kw dual channel het in the framework of the esa tandem project. In *38th International Electric Propulsion Conference Proceedings*, 2024.

[42]F. Marconcini, G. Giammarinaro, G. Becatti, M. M. Saravia, C. Guidi, F. Paganucci, F. Dini, F. Scortecci, and D. Estublier. A 20 kw magnetically shielded nested hall thruster: Status and perspectives of the tandem project. In *Space Propulsion 2024*, 2024.